



Inefficient Growth of SiO_x Grains: Implications for Circumstellar Outflows

Yuki Kimura¹ , Kyoko K. Tanaka² , Yuko Inatomi^{3,4} , Frank T. Ferguson^{5,6} , and Joseph A. Nuth, III⁵

¹ Institute of Low Temperature Science, Hokkaido University, Kita-19, Nishi-8, Kita-ku, Sapporo 060-0819, Japan; ykimura@lowtem.hokudai.ac.jp

² Astronomical Institute, Tohoku University, 6-3 Aoba, Aoba-ku, Sendai 985-8578, Japan

³ Institute of Space and Astronautical Science, Japan Aerospace Exploration Agency, 3-1-1 Yoshinodai, Chuo-ku, Sagami-hara, Kanagawa 252-5210, Japan

⁴ School of Physical Sciences, SOKENDAI (Graduate University for Advanced Studies), 3-1-1 Yoshinodai, Chuo-ku, Sagami-hara, Kanagawa 252-5210, Japan

⁵ NASA Goddard Space Flight Center, 8801 Greenbelt Road, Greenbelt, MD 20071, USA

⁶ Catholic University of America, 620 Michigan Avenue, Washington, DC 20064, USA

Received 2022 May 17; revised 2022 June 17; accepted 2022 July 7; published 2022 July 22

Abstract

To explain observations of abundant circumstellar dust and high stellar wind velocity, most models simply postulate the efficient nucleation and growth of silicate dust particles. Here, we report measurement of the SiO–(SiO_x)_n grain sticking coefficient in a microgravity sounding rocket experiment, indicating very inefficient (0.005–0.016) grain formation from the vapor. Application of this measurement to radiative-driven winds in oxygen-rich asymptotic giant branch stars indicates that the initial grain condensate population should consist of very tiny dust particles in very large numbers. Aggregation of this dust population will produce low-dimension fractal aggregates that should couple well to the stellar radiation field and efficiently drive stellar mass loss.

Unified Astronomy Thesaurus concepts: [Circumstellar dust \(236\)](#)

1. Introduction

Circumstellar outflows from oxygen-rich asymptotic giant branch (AGB) stars are driven by stellar radiation pressure on silicate grains (Woolf & Ney 1969; Waters et al. 1996; Kemper et al. 2001; Nuth & Johnson 2006). Such grains do not exist in the atmospheres of AGB stars but must first nucleate and grow from gas-phase constituents, primarily SiO, Mg, Fe, and oxygen in the form of O, OH, and H₂O (Gail & Sedlmayr 1986, 1999). This process occurs in three distinct, potentially overlapping phases: nucleation, growth, and aggregation. It is also possible that in some stars silicate grains will be thermally annealed from the initially amorphous condensates to more ordered, crystalline minerals, though this latter process only occurs in high mass-loss-rate stars (Hallenbeck et al. 2000).

Nucleation is the process by which SiO gas undergoes a phase change to a liquid or solid (Becker & Döring 1935; Zel'dovich 1942; Feder et al. 1966). The change proceeds through a distribution of increasingly complex and less thermodynamically stable gas-phase clusters until the addition of an SiO monomer finally increases, rather than decreases, the stability of the growing cluster. This transition occurs at what is called the “critical cluster size.” The details of clustering processes of SiO molecules has also been theoretically demonstrated by quantum chemical modeling (Reber et al. 2008; Goumans & Bromley 2012; Bromley et al. 2016). There was some question as to whether a distribution of precondensation clusters would be near equilibrium in a circumstellar environment (Donn & Nuth 1985) and potentially invalidate classical nucleation theory (Becker & Döring 1935; Zel'dovich 1942; Feder et al. 1966). However, a subsequent study (Paquette & Nuth 2011) demonstrated that even if these cluster distributions were not in local thermal equilibrium and their concentration was suppressed by several orders of magnitude this had little effect on grain formation in an

outflow except to move the point of nucleation slightly further out in the shell.

Once grain nuclei form, they begin to grow. If growth is efficient then gas-phase SiO is rapidly depleted and nucleation ends. If growth is inefficient, nucleation continues together with grain growth until SiO is depleted, with the result that many tiny grains form rather than fewer larger ones (Nuth et al. 2020). Some recent models of radiation-driven circumstellar winds (Höfner 2008; Bladh & Höfner 2012; Bladh et al. 2015, 2019) require that magnesium silicate grains grow to micron scale to efficiently couple to the stellar radiation field. Such models simply postulate the formation of seed nuclei that grow very efficiently (e.g., each collision adds an SiO or Mg atom to the growing seed).

2. Experimental Procedure

We report the results of a Black Brant IX sounding rocket experiment (launched at 11:00 a.m. EDT on 2019 October 7 from White Sands, New Mexico) in which SiO nucleation and growth in an argon atmosphere was observed in microgravity starting from a vapor generated by evaporation of silica deposited on a heated tantalum wire. Note that the composition of the silica of the evaporation source may not be completely SiO₂ and “silica” is used in the sense of SiO_x in this Letter. The temperature and concentration of evaporated SiO molecules at the point of nucleation were determined using a double-wavelength Mach–Zehnder-type laser interferometer (Figure 1). The supersaturation of SiO in the evaporated vapor as well as in the gas outflow from the mass-losing star increases as gas cools and then SiO nucleates (see the [Appendix](#) materials). The ratio between collision frequency of SiO molecules and the increase in supersaturation is comparable between the experiment and the mass-losing star (Yamamoto & Hasegawa 1977; Nozawa & Kozasa 2013). Therefore, the condensation temperature in our experiment should be close to that of SiO in the gas outflow of evolved stars. This is one of the advantages of the microgravity experiment, because the timescale of the supersaturation increase is much shorter in ground-based experiments (Kimura & Tsukamoto 2017). Other advantages of the microgravity experiment are discussed in the



Original content from this work may be used under the terms of the [Creative Commons Attribution 4.0 licence](#). Any further distribution of this work must maintain attribution to the author(s) and the title of the work, journal citation and DOI.

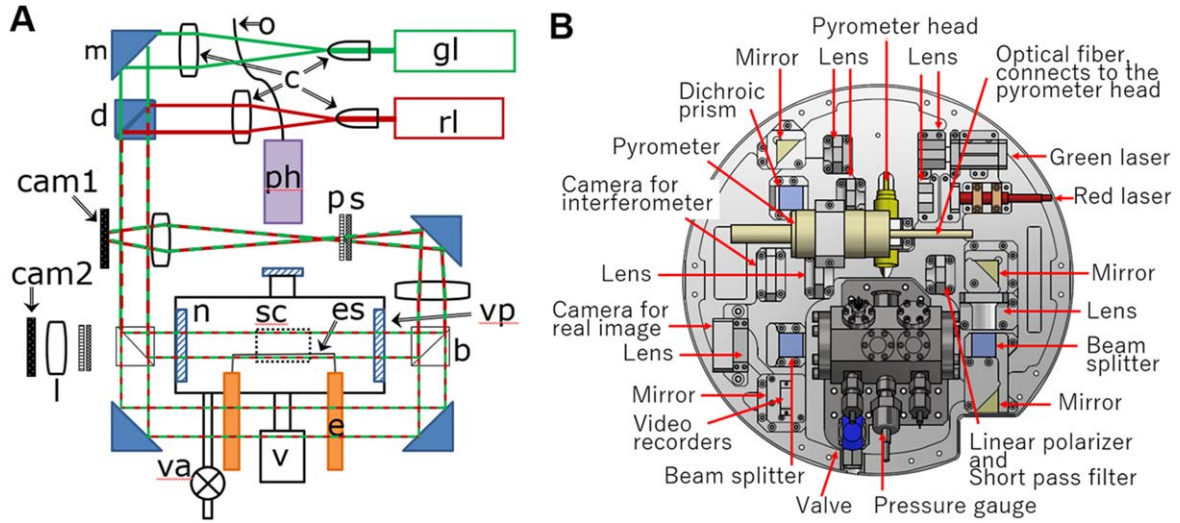


Figure 1. Schematics of the experimental system. (A) Configuration and optical path of the double-wavelength, Mach-Zehnder-type laser interferometer and the nucleation chamber. The red and green lines show the optical paths of the red and green lasers, respectively. The interference fringes and real image are recorded with CMOS cameras (cam 1 and 2, respectively). The evaporation source and a sample collector are shown as the black solid (es) and dotted (sc) lines, respectively, in the nucleation chamber (n). The other labels are as follows: b, beam splitter; c, collimator; d, dichroic mirror; e, electrode; l, lens; m, mirror; o, optical fiber; p, polarizer; s, short-pass filter; v, vacuum gauge; gl, green laser; ph, pyrometer head; rl, red laser; va, valve with a gas line; vp, view port. (B) Top view in drawing by three-dimensional CAD. All optics and the chamber are on a base plate of ϕ 405 mm.

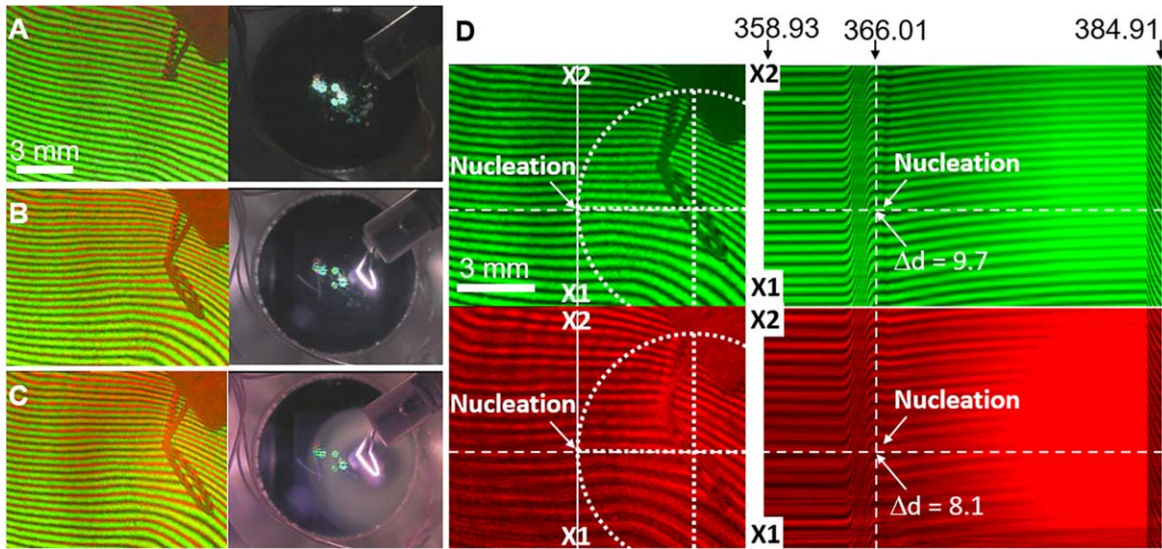


Figure 2. Snapshots of in situ observations at the moment of nucleation of SiO from hot vapor. Left and right panels show double-wavelength interference fringes and the real image, respectively, (A) before heating ($T+358.94$ s), (B) just before nucleation ($T+366.01$ s), and (C) during nucleation ($T+366.88$ s). T is time of launch. The 0.2 mm diameter Ta rod is connected to Cu electrodes (ϕ 6.0 mm). (D) Color-separated interference fringes of panel (C) and corresponding time series images at the position indicated by white lines from 5 s before heating. The vertical dashed line and horizontal and vertical axes in the time series images are the time of nucleation and time from 358.93 to 384.91 s and position from X1 to X2, respectively. The center of the dotted circle, 4.5 mm in radius, is approximately at the center of evaporation as seen in the right plot of panel (C).

Appendix materials. The particle composition, structure, and grain size distribution were measured after payload recovery using a transmission electron microscope (TEM; JEM-2100F, JEOL Ltd., Tokyo). The results were analyzed by calculations of the condensation process using Modified Classical Nucleation Theory (MCNT; Tanaka et al. 2002).

3. Experimental Results

When the Ta wire was electrically heated 363.94 s after launch ($T+363.94$), interference fringes around the evaporation source were shifted due to the decreasing density of the Ar by thermal heating (Figure 2). The deviation of the fringes depends on the

temperature. Once SiO evaporates, shifts in the interference fringes also depend on the concentration of SiO molecules. The temperature and concentration of SiO molecules can be determined simultaneously based on the deviations of the interference fringes of the two lasers (Figure 3), which can be calculated for the red and green (Figure 2(D)) lines using the refractive indices of Ar (Clergent et al. 1999) and SiO (Hass & Salzberg 1954). While the concentration of SiO can be affected by the generation of other molecules such as O_2 , OH, H_2O , or H_2 , the influence of those molecules is assumed to be negligible to determine partial pressure of SiO: the refractive indices of O_2 , H_2O , or H_2 are much smaller than that of SiO (30%, 28%, and 15% of SiO, respectively).

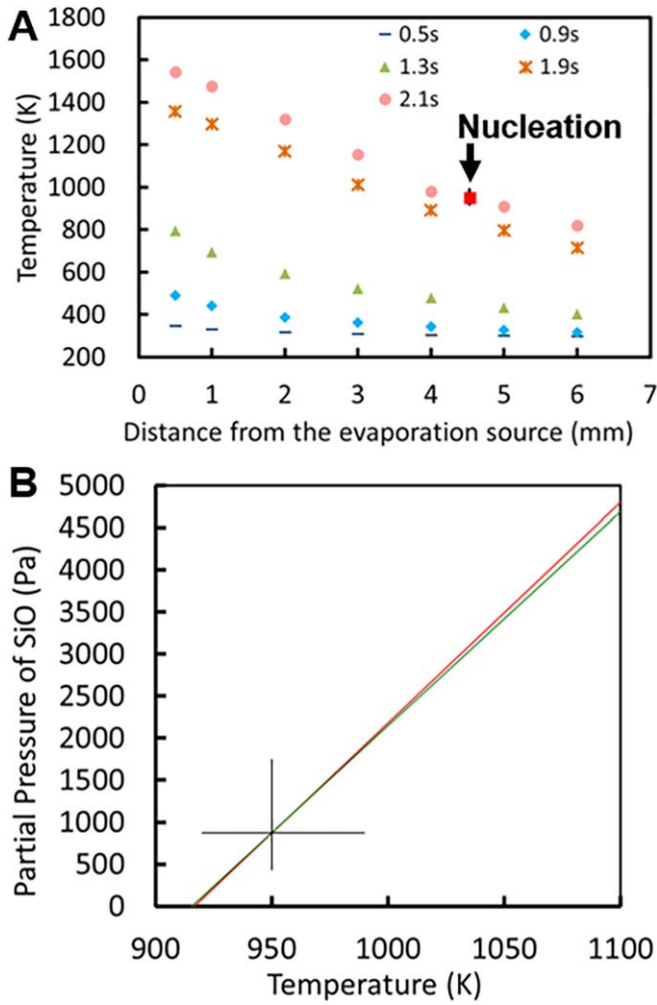


Figure 3. Temperature profile and SiO concentration at nucleation. (A) Temperature distribution in terms of the distance from the evaporation source in time after the start of heating. The bar, diamond, triangle, star, and circle symbols show 0.5, 0.9, 1.3, 1.9, and 2.1 s after the start of heating of the evaporation source, respectively. The red square at 4.5 s shows the nucleation point and temperature. (B) The black cross shows the temperature and concentration of SiO molecules just before nucleation. The green and red lines show the relationship between the temperature and the concentration of the SiO molecule to explain the deviations in the interference fringes for the green and red lasers, respectively.

Therefore, even if the gas contains other gases at concentrations as much as 10% of SiO, the effect on the calculation of the concentration of SiO is small, only a few percent.

After 2.94 s from the start of electrical heating ($T+366.88$), SiO smoke composed of nanometer-sized silica particles can be seen 4.5–5.2 mm from the evaporation source in both the interference and real images (Figure 2(C)). The temperature and concentration of SiO molecules just before nucleation are 950^{+40}_{-30} K and 873^{+873}_{-437} Pa, respectively (Figure 3(B)). The relatively large error is due to the broadening of the evaporation center by thermal expansion of the Ta rod (Figures 2(B) and (C)). According to the equilibrium vapor pressure equation of SiO (P_{SiO} ; Ferguson & Nuth 2008),

$$\log P_{\text{SiO}} = (13.29 \pm 0.39) - \frac{17740 \pm 550}{T}, \quad (1)$$

where T is absolute temperature; the equilibrium vapor pressure at the nucleation temperature is 4.1×10^{-6} (4.4×10^{-7} – 3.8×10^{-5})

Pa. Therefore, the supersaturation ratio is as large as 2.1×10^8 . There are other experimental measurements of the vapor pressure of SiO. The vapor pressure in Equation (1) is consistent with that in Wetzel et al. (2012) within the error bars, and the error bars are smaller. Gail et al. (2013) report a smaller vapor pressure, but the value is much smaller than the partial pressure in Equation (1) at the same temperature as the evaporation source temperature. The reason may be the dependence of the SiO vapor pressure on diffusion through the ambient gas.

The nucleation temperature of 950^{+40}_{-30} K is consistent with the temperature of 900–1200 K in a stellar outflow, where dust formation has been expected (e.g., Jeong et al. 2003). It is possible that Ar, which is introduced in the nucleation chamber as a buffer gas, plays a role in the three-body collision and facilitates nucleation, though hydrogen in the outflows should also be effective in this role. Since the nucleation temperature in this experiment corresponds to the lower limit of the observation, the extent to which Ar gas facilitates nucleation is not considered to be significant. No effect of Ar was observed in the Fe nucleation experiments at different Ar gas pressures (Kimura et al. 2017). Thus, dimer formation has the largest energy barrier in the formation of iron grains. In the case of SiO, theoretical calculations have shown that the energy barrier for dimer formation is small (Avramov et al. 2005), and experiments have shown that SiO oligomerization proceeds even in low-temperature He droplets (Krasnokutski et al. 2014). The bonding energy for dimerization of SiO may be absorbed by the vibration of the Si–O bond and, therefore, the role of a third body might not be significant in the nucleation of SiO.

Particles produced in the experiment are amorphous silica with a mean diameter of 24.4 nm (18.4 nm median diameter) and the Si/O ratio is 3/4 (Figure 4). Note that the quantitative accuracy of oxygen in the energy dispersive X-ray analysis of TEM is not high. There was no significant signal from other elements except Mo originating from the TEM grid.

4. Physical Quantities for SiO_x Grain Formation

To interpret the nucleation condition, a sticking probability α and surface tension σ for SiO grain formation are determined (Figure 5) based on numerical calculations of the none-equilibrium condensation of SiO using the MCNT (see the Appendix materials). Figure 5 shows the mean particle radius and nucleation temperature obtained from the calculations using various α and σ .

Figure 6 shows the result of a simulation with a sticking probability $\alpha = 1.6 \times 10^{-2}$ and surface tension $\sigma = 1.33 \text{ N m}^{-1}$ (1330 erg cm^{-1}). As evaporated SiO vapor cools, the nucleation rate increases significantly because of the increase in the supersaturation ratio. Then, the number density of the SiO molecules decreases from the vapor and the nucleation rate decreases rapidly. The nucleation rate reaches a maximum at ~ 980 K, and the nucleation temperature (where half of the initial gas-phase SiO molecules are consumed) has been represented at 950 K (Figure 6(A)). If we assume $\alpha = 1$, the model nucleation temperature is expected to be 1095 K, which is far from the experimental result. The mean radius of the silica particles increases gradually at the beginning (Figure 6(B)) because of continuous formation of tiny new particles by nucleation, which works to suppress the growth rate in the mean particle radii. Once the nucleation rate passes the peak, most remaining SiO

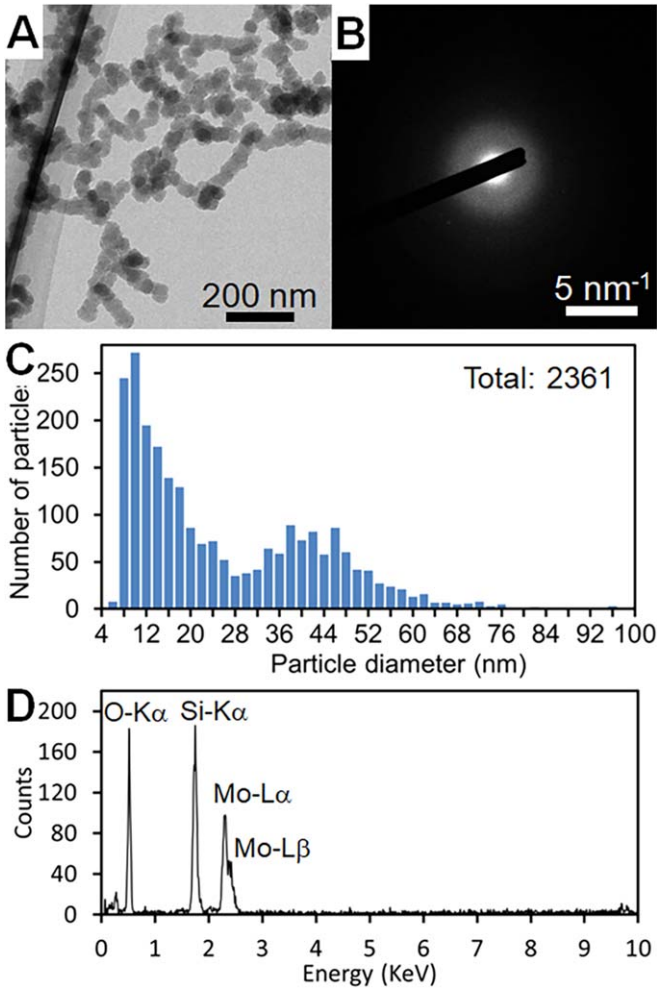


Figure 4. Particle characteristics. (A) Bright field TEM image of SiO grains. (B) Corresponding electron diffraction pattern of panel (A) indicates the amorphous structure of the SiO particles. (C) Size distribution of SiO grains. The median and mean diameters are 18.4 nm and 24.4 nm, respectively; 95% of particles are in the range of 8–56 nm. (D) Energy dispersive X-ray spectrum of the particles suggests that the atomic ratio of silicon and oxygen is Si/O = 3/4.

molecules are consumed by growth and a smaller fraction of newly formed nuclei, because the supersaturation ratio becomes too small to support nucleation. Then, the mean radius increases faster. Since there is a finite concentration of SiO in the gas, more nuclei lead to smaller average particles for the same level of SiO depletion since the SiO is spread out over a larger number of particles.

The sticking probability and surface tension are determined from the nucleation temperature and final particle size. Although the sticking probability should have size dependence, we could determine only an averaged value from the SiO monomer to the final grain size. Note that the size of a critical nucleus can be estimated to be approximately five SiO molecules by MCNT. So the vast majority of “sticking” occurs during growth from the critical cluster size up to the final grain size. In the clustering of SiO molecules, it has been theoretically shown that the monocyclic structures are relatively stable up to the tetramer, while the more complex forms, such as double cyclic structures or three-dimensional structures, become more stable structure from the pentamer onward (Bromley et al. 2016). When a SiO cluster becomes a pentamer, the Si–Si bond appears for the first time,

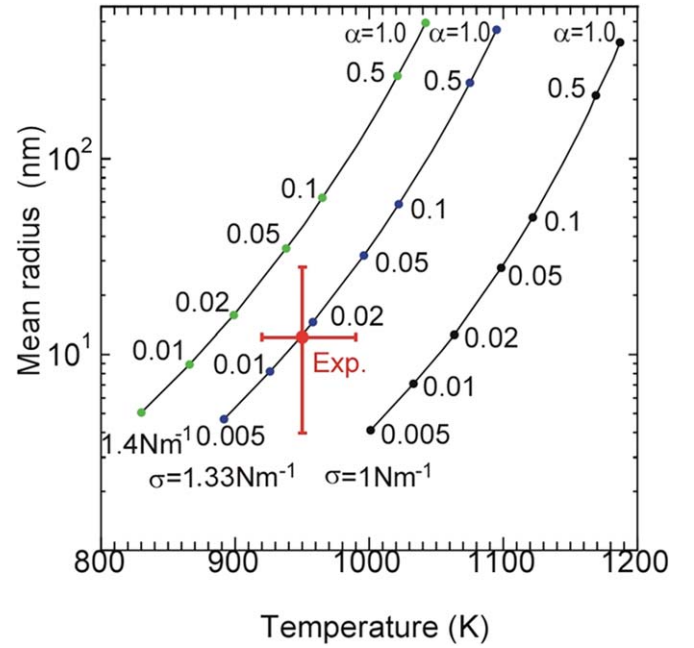


Figure 5. Plots of sticking probabilities and surface tensions regarding the nucleation temperature and mean radius using MCNT. Each line shows the mean particle radius and condensation temperature obtained from the calculations when the surface tension is 1.0, 1.33, and 1.4 N m^{−1}, respectively. The numbers of points on the line indicate the value of α used in the calculations. The sticking probability and surface tension to explain the experimental results, which are the nucleation temperature of 950 K and mean radius of 12.2 nm, are $\alpha = 1.6 \times 10^{-2}$ and $\sigma = 1.33$ N m^{−1} (1330 erg cm^{−1}), respectively. The error bar on the y-axis includes a size range of 95% of the particles, 4–28 nm in radius.

causing oxygen bias in the cluster. Once a Si–Si bond forms, an oxygen atom adds by breaking the Si–Si bond and forms a SiO₂ unit (Reber et al. 2008). The relevance of these theoretical reports to the present experimental results, in which the critical nucleus size is five SiO molecules, is left to future research.

As can be seen from Figure 5, the average sticking coefficient for a gas-phase SiO molecule colliding with a growing silicate grain is ~ 0.016 . In other words, for every 100 SiO molecules that collide with a growing grain only one or two are captured. In the only two previous studies of the growth of solid particles from the gas phase the calculated sticking coefficients were much lower. For zinc atoms colliding with zinc crystals only 3 out of 100,000 collisions resulted in grain growth (Michael et al. 2003). Iron atoms colliding with growing iron particles similarly showed an efficiency of ~ 0.00002 (Kimura et al. 2017). For zinc, we can explain inefficient growth due to the difficulty of the colliding atom coming upon a vacancy in the growing crystal lattice before it evaporates from the grain surface. The much higher sticking coefficient of SiO molecules on silica grains is reasonable because the silica grains are highly amorphous or glassy and therefore provide a much higher defect density where SiO molecules can be captured into the grains.

In the case of a similar Fe experiment, the critical cluster was the dimer. In this case the forming dimer returns to the vapor phase by dissociation due to the excess energy from the formation of the Fe–Fe bond. Therefore, in the case of isolated atoms, the formation of dimers can present the largest barrier to grain nucleation. In the case of SiO, formation of the dimer is relatively easy compared with that of single element such as Zn and Fe, and therefore it is not the greatest hindrance for nucleation. In addition to the growth process, the nucleation

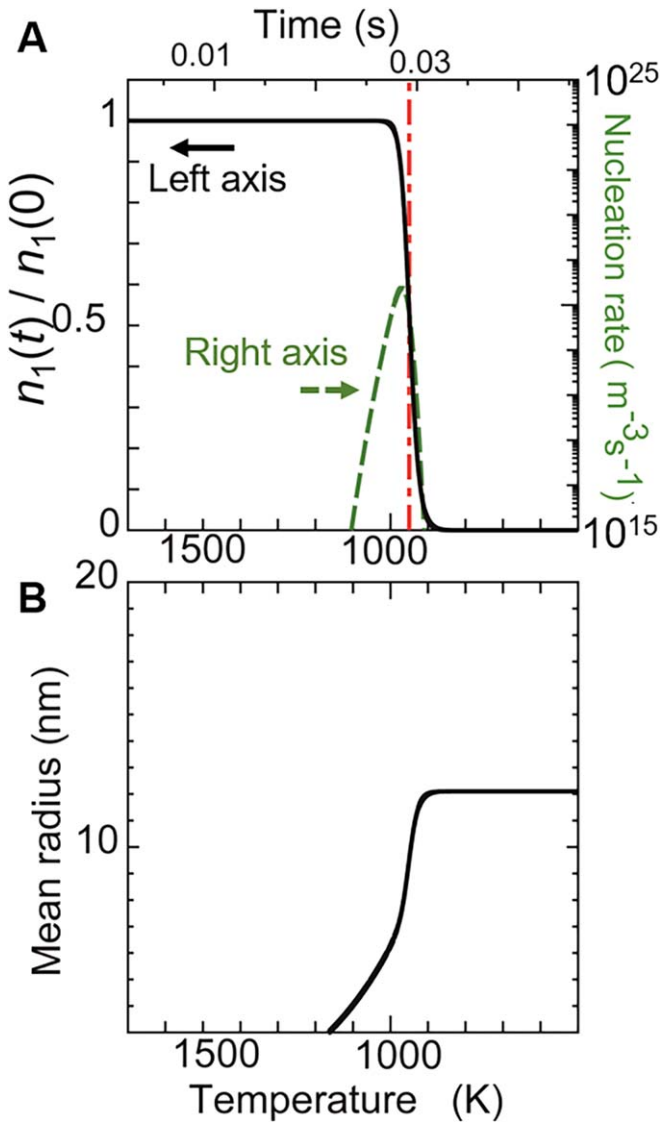


Figure 6. MCNT calculated results for the formation of silica grains. (A) The dashed and solid curves show the time variation in the nucleation rate and the number density of gas-phase SiO molecules $n_1(t)$, respectively, in the case of a sticking probability of $\alpha = 1.6 \times 10^{-2}$ and a surface tension of $\sigma = 1.33 \text{ N m}^{-1}$ (1330 erg cm^{-1}). The vertical dotted line shows the nucleation temperature derived from the experiment. (B) Growth curve of a typical SiO grain.

process also suggests a relatively more efficient sticking of SiO and therefore more efficient formation of silica grains compared to that of metallic grains.

We should note that the measured sticking probability is likely an overestimate. The volume of SiO monomers compared to the total grain volume was used in the analysis above to calculate how many SiO molecules were incorporated into a growing grain, compared to the number of SiO molecules that collided with the grain during growth. However, the final silica grains are more than just a collection of SiO monomers as energy dispersive X-ray spectroscopy analysis in Figure 4(D) suggests that their composition is actually $\text{SiO}_{1.3}$. These grains contain extra oxygen from reactions with oxygen from the evaporating silica. In short, the volume of the final grains is larger than the actual number of SiO molecules that were incorporated into them due to the addition of this extra oxygen. In addition, double peaks in the size distribution in Figure 4(C)

may be due to the fusion growth of smaller particles. Namely, the larger peak may be produced by secondary growth due to the merger of two or more earlier formed smaller particles, thus, artificially inflating the collisional growth efficiency of the grain growth process by a small numerical factor. If the size of the primary particle is $\sim 10 \text{ nm}$ in diameter, which is the peak of the size distribution of smaller particles, the sticking probability can be as small as ~ 0.005 . This is a reasonable lower limit to the sticking probability derived from this experiment.

5. Astronomical Implications

In a circumstellar environment both atomic magnesium and iron also contribute to grain growth, though no measurement of the efficiency of their incorporation into growing silicate grains is yet available. Previous studies of the vapor-phase nucleation of SiO (Nuth & Donn 1982) and SiO plus Mg (Nuth & Donn 1983) suggest that the grain formation rate is controlled by formation of pure $(\text{SiO})_x$ clusters that then grow by the addition of SiO, Mg, and oxygen. Therefore, the number density of silica nuclei controls the size distribution of silicate grains.

In the case of where less SiO is in the gas outflow, other refractory dust, such as aluminum or titanium oxides, might be condensed earlier than silicate, and, then, condensation of silicate might proceed via heterogeneous nucleation on the surfaces of these refractory dust (e.g., Kozasa & Sogawa 1997; Karovicova et al. 2013). To discuss the condensation sequences more quantitatively, we need additional data regarding the formation efficiency of other refractory dust species.

Inefficient grain growth retards the depletion of SiO monomers from the gas phase and therefore prolongs the nucleation process, resulting in more $(\text{SiO})_x$ critical clusters (Gerlach 1969). Growth of this much larger population of seed nuclei rapidly produces orders of magnitude more small grains when the gas phase is finally depleted of condensable material. Note that the relative number of small grains produced from a given quantity of refractory vapor is proportional to the ratio of the grain radii cubed. The high density of small grains promotes aggregation. Aggregation in circumstellar outflows should produce a population of fractal grains with fractal dimension less than 2 (Wurm & Blum 1998; Tazaki et al. 2016). For such fractal aggregates each of the constituent grains remains fully coupled to both the radiation field and to the gas (Meakin & Donn 1988). So, while the radiative coupling for each individual grain might decrease due to their small size, the number of grains vastly increases, potentially resulting in a much larger overall coupling of the stellar radiation field (per unit mass of dust) to the wind. We note that the structure of the grains formed in this experiment (see Figure 4(A)) is consistent with the formation of very open fractal aggregates even at the much higher grain densities in the rocket experimental chamber compared to those in circumstellar outflows.

J.A.N. and F.T.F. gratefully acknowledge the support of the NASA Sounding Rocket Program. Developments of the experimental system were supported by the Technical Division of Institute of Low Temperature Science, Hokkaido University, and the Advanced Machining Technology Group of JAXA. Onboard data saving was supported by Dr. S. Takeuchi of ISAS/JAXA. This work was partly supported by Grant-in-Aids for Scientific Research (S) from KAKENHI (15H05731 and 20H05657).

Appendix

Materials and methods. A silica coating with $\sim 5 \mu\text{m}$ thickness was prepared on a Ta rod ($\phi 0.2 \times 70 \text{ mm}$) as an evaporant. This was prepared by coating the surface of a Ta wire with tetraethyl orthosilicate-like material and then calcining it (Tocalo Co. Ltd.). The Ta rod was set in a nucleation chamber (135 mm-long stainless-steel cylinder) with a volume of $\sim 500 \text{ ml}$. The chamber has a pressure gauge (HAV-60KP-V, Sensez Co., Tokyo) and a pyrometer (ISQ5-LO/MB25, Yamari Industries Ltd., Yokohama) to measure total pressure in the chamber and the temperature of the evaporation source, respectively (Figure 1). To simulate the condensation of silica dust from a cooling gas, hot SiO vapor was generated by the evaporation of the silica by electrical heating of the Ta rod in the nucleation chamber filled with 40,000 Pa of Ar gas ($>99.9999\%$ purity) to shorten the mean free path. This enabled us to reduce the physical size of the experimental system, the timescale for nucleation and growth of particles, and the cooling of the gas. The silica particles produced in the experiment were directly deposited on a standard Mo grid with plastic frames coated by carbon (called a microgrid) for TEM measurement $\sim 30 \text{ mm}$ from the evaporation source. The temperature of the sample collector was measured using a platinum resistance thermometer (Pt100, type MC-0805, Netsushin Co., Ltd.). The temperature of the collector did not exceed 40°C (the initial temperature was 20.5°C).

The temperature and concentration of evaporated SiO molecules were determined from the deviations of the interference fringes measured by a Mach–Zehnder-type interferometer, which has two polarized red (635 nm) and green (532 nm) lasers (Figure 1). Silica was evaporated concentrically from the Ta rod (68.6 mm long) to make a cylindrical cloud of hot vapor. The two lasers pass through the chamber in parallel with the Ta rod and cylindrical vapor cloud. The interference fringes and real images were observed by CMOS cameras (MS-M213FHS without a low-pass filter and MS-M33WT3, respectively, Moswell Co., Ltd., Yokohama) and recorded at 30 frames s^{-1} .

The particles collected on the TEM grids were directly loaded into a TEM (JEM-2100F, JEOL Co., Tokyo), and the particle size distribution was measured. The elemental ratio of silicon and oxygen was measured using an energy dispersive X-ray analysis system (JED-2300 Series, JEOL Co., Tokyo) installed on the TEM.

Numerical calculations using the MCNT. We apply the MCNT, which modifies the classical nucleation theory by adding an extra term in the free energy term for cluster formation to satisfy that the free energy of the monomer is zero (Tanaka et al. 2014). The nucleation rate J is given by

$$J = \left\{ \sum_{i=1}^{\infty} \frac{1}{R^+(i)n_e(i)} \right\}^{-1}, \quad (\text{A1})$$

where $n_e(i)$ is the equilibrium number density of i -mers (clusters containing i atoms) and $R^+(i)$ is the accretion rate from an i -mer to an $(i+1)$ -mer which is expressed as

$$R^+(i) = \alpha n_1 v_{\text{th}} (4\pi r_1^2 i^{\frac{2}{3}}), \quad (\text{A2})$$

where n_1 is the number density of SiO molecules, v_{th} is the thermal velocity of gas given by $\sqrt{kT/(2\pi m)}$, and α is the sticking probability. The radius of a molecule r_1 is defined as $(3m/4\pi\rho_m)^{1/3}$, where m ($=7.3 \times 10^{-23} \text{ g}$) is the mass of a

molecule and ρ_m ($=2.3 \text{ g cm}^{-3}$) is the bulk density. The equilibrium number density of i -mers $n_e(i)$ is given by

$$n_e(i) = \frac{P}{kT} \exp\left(-\frac{\Delta G_i}{kT}\right), \quad (\text{A3})$$

where P is the partial pressure of SiO gas, k is the Boltzmann constant, and ΔG_i is the free energy associated with the formation of a cluster of size i from the gas phase. ΔG_i by the MCNT model is expressed as

$$\Delta G_i = -(i-1)kT \ln S + \sigma A_1(i^{\frac{2}{3}} - 1), \quad (\text{A4})$$

where S ($=P/P_{\text{SiO}}$) is the supersaturation ratio, σ is the surface tension, and A_1 ($=4\pi r_1^2$) is the surface area of a monomer. The equilibrium vapor pressure of SiO materials P_{SiO} is given by Equation (1).

As shown above, the nucleation rate is determined by various quantities such as temperature, partial pressure of SiO vapor, surface tension σ , and sticking probability α . Since we know all the physical quantities except σ and α , we can obtain the values of σ and α by fitting the nucleation temperature and mean particle radius obtained by the experiments.

To interpret the results of our experiments, we performed numerical calculations of the nonequilibrium condensation of SiO based on the nucleation theory (Tanaka et al. 2002; Kimura et al. 2017). In the calculation, we adopted the initial temperature of 1770 K. The timescale for cooling τ_T was taken as the time required for the SiO gas to arrive at the nucleation site by diffusion from the evaporation source: $\tau_T \approx X^2 D^{-1}$, where X is the distance from the evaporation source to the nucleation site ($X = 0.453 \text{ cm}$), and D ($=5.66 \text{ cm}^2 \text{ s}^{-1}$) is the diffusion coefficient. The obtained timescale for cooling is $\tau_T = 3.63 \times 10^{-2} \text{ s}$. In the estimation, we use the diffusion coefficient given by $D = v_{\text{mean}} l/3$, where $v_{\text{mean}} = 8.09 \times 10^4 \text{ cm s}^{-1}$ is the mean velocity of the gas with the mean temperature 1360 K between the evaporation source and the nucleation site. l is the mean free path of a gas molecule given by $(\sqrt{2}ns)^{-1} = 2.10 \times 10^{-4} \text{ cm}$, where we use the cross section of a SiO atom $s = 1.28 \times 10^{-15} \text{ cm}^2$ and the number density of total gas $n = 2.47 \times 10^{18} \text{ cm}^{-3}$ from the total gas pressure measured in the experiment (49510 Pa at the time of nucleation).

In the calculation, the nucleation temperature has been defined as the point at which half of the initial gas-phase SiO molecules are consumed, as shown by the vertical dotted line in Figure 6(A). After this point the peak of the nucleation rate is passed, and the number of newly formed nuclei decreases. In addition, if no additional nuclei form after the vertical dotted line, the average particle has already grown to 19.4 nm in diameter, which is very close to the 24.4 nm mean diameter of the collected particles. This is consistent with the experimental detection at the moment of nucleation from the scattering of laser light in the interference image and the radiation from the evaporation source in the real image.

Advantages of the microgravity experiments: In the aggregation processes of atoms and molecules under terrestrial gravity, although the effect of gravity on individual atoms and molecules is small, macroscopic convections are induced by concentration and temperature gradients in the gas atmosphere. Density-differential convection leads to differences in cooling rates and heterogeneity in the nucleation environment. In fluid mechanics, systems with the same Reynolds number can be regarded as physically equivalent. Similarly, it is known that the formation process of cosmic dust can be regarded as equivalent when the





relationship between timescale of supersaturation increases and the collision frequency is comparable (Yamamoto & Hasegawa 1977; Nozawa & Kozasa 2013). While ground-based experiments can reproduce dust formation around novae, it is difficult to reproduce the conditions for dust formation in the gas outflow from supernovae and late-type giants, which are considered to be the main current sources of cosmic dust. In the case of microgravity experiments, density-difference convection is negligibly weak, and thus the experiments are analogous to the formation environment of cosmic dust in the gas outflow from supernovae and late-type giant stars. Therefore, the nucleation temperature of the microgravity experiment can be directly compared with that of the observation (Kimura & Tsukamoto 2017). As a result, the physical constants under the temperature and supersaturation conditions in the actual nucleation environment can be obtained, which can be a crucial factor to elucidate the formation process of cosmic dust.

The absence of density-difference convection means that the Reynolds number is small, and the environment is less prone to turbulence. Density fluctuations induce nucleation, as evidenced by the fact that crystallization initiates when super-cooled water is shaken. In the microgravity environment, the density fluctuations are relatively small, and the sticking probability and surface free energy can be determined more accurately than in ground-based experiments.

In ground-based experiments, the fusion growth of particles in density-differential convection may be enhanced, leading to an increase in particle size. Since the sticking probability and surface free energy are constrained from the nucleation temperature and the measured particle size, the increase in the produced final particle size due to fusion growth risks overestimating the sticking coefficient.

The evaporated material diffuses evenly around the evaporation source. In the presence of convection, the evaporated gas is quenched and nucleated at a higher concentration in the lower part of the evaporation source, while it is nucleated at a relatively lower concentration in the upper part under a gentler temperature gradient. As a result of the heterogeneity of the nucleation environment, the size distribution of the final particles widens. This leads to an increase in the sticking probability and surface free energy error bars.

ORCID iDs

Yuki Kimura  <https://orcid.org/0000-0002-9218-7663>
 Kyoko K. Tanaka  <https://orcid.org/0000-0002-3555-7891>
 Yuko Inatomi  <https://orcid.org/0000-0002-2845-9636>
 Frank T. Ferguson  <https://orcid.org/0000-0002-9395-3825>

References

- Avramov, P. V., Adamovic, I., Ho, K.-M., et al. 2005, *JPCA*, **109**, 6294
 Becker, Von R., & Döring, W. 1935, *AnP*, **416**, 719
 Bladh, S., & Höfner, S. 2012, *A&A*, **546**, A76
 Bladh, S., Höfner, S., Aringer, B., & Eriksson, K. 2015, *A&A*, **575**, A105
 Bladh, S., Liljegren, S., Höfner, S., Aringer, B., & Marigo, P. 2019, *A&A*, **626**, A100
 Bromley, S. T., Martin, J. C. G., & Plane, J. M. C. 2016, *PCCP*, **18**, 26913
 Clergent, Y., Durou, C., & Laurens, M. 1999, *J. Chem. Eng. Data*, **44**, 197
 Donn, B., & Nuth, J. A. 1985, *ApJ*, **288**, 187
 Feder, J., Russel, K. C., Lothe, J., & Pound, G. M. 1966, *AdPhy*, **15**, 111
 Ferguson, F. T., & Nuth, J. A. 2008, *J. Chem. Eng. Data*, **53**, 2824
 Gail, H. P., & Sedlmayr, E. 1986, *A&A*, **166**, 225
 Gail, H. P., & Sedlmayr, E. 1999, *A&A*, **347**, 594
 Gail, H.-P., Wetzell, S., Pucci, A., & Tamanai, A. 2013, *A&A*, **555**, A119
 Gerlach, R. L. 1969, *JChPh*, **51**, 2186
 Goumans, T. P. M., & Bromley, S. T. 2012, *MNRAS*, **420**, 3344
 Hallenbeck, S. L., Nuth, J. A., III, & Nelson, R. N. 2000, *ApJ*, **535**, 247
 Hass, G., & Salzberg, C. D. 1954, *JOSA*, **44**, 181
 Höfner, S. 2008, *A&A*, **491**, L1
 Jeong, K. S., Winters, J. M., Le Bertre, T., & Sedlmayr, E. 2003, *A&A*, **407**, 191
 Karovicova, I., Wittkowski, M., Ohnaka, K., et al. 2013, *A&A*, **560**, A75
 Kemper, F., Waters, L. B. F. M., de Koter, A., & Tielens, A. G. G. M. 2001, *A&A*, **369**, 132
 Kimura, Y., Tanaka, K. K., Nozawa, T., Takeuchi, S., & Inatomi, Y. 2017, *SciA*, **3**, 1601992
 Kimura, Y., & Tsukamoto, K. 2017, in *New Perspectives on Mineral Nucleation and Growth*, ed. A. E. S. Van Driessche et al. (Cham: Springer), 339
 Kozasa, T., & Sogawa, H. 1997, *Ap&SS*, **251**, 165
 Krasnokutski, S. A., Rouillé, G., Jäger, C., et al. 2014, *ApJ*, **782**, 15
 Meakin, P., & Donn, B. 1988, *ApJ*, **329**, L39
 Michael, B. P., Lilleleht, L. U., & Nuth, J. A. 2003, *ApJ*, **590**, 579
 Nozawa, T., & Kozasa, T. 2013, *ApJ*, **776**, 24
 Nuth, J. A., & Donn, B. 1982, *JChPh*, **77**, 2639
 Nuth, J. A., & Donn, B. 1983, *JChPh*, **78**, 1618
 Nuth, J. A., Ferguson, F. T., Homan, W., Decin, L., & Paquette, J. A. 2020, *ApJ*, **901**, 144
 Nuth, J. A., & Johnson, N. M. 2006, *Icar*, **180**, 243
 Paquette, J. A., & Nuth, J. A. 2011, *ApJL*, **737**, L6
 Reber, A. C., Paranthaman, S., Clayborne, P. A., Khanna, S. N., & Castleman, Jr., A. W. 2008, *ACS Nano*, **2**, 1729
 Tanaka, K. K., Diemand, J., Angelil, R., & Tanaka, H. 2014, *JChPh*, **140**, 194310
 Tanaka, K. K., Tanaka, H., & Nakazawa, K. 2002, *Icar*, **160**, 197
 Tazaki, R., Tanaka, H., Okuzumi, S., Kataoka, A., & Nomura, H. 2016, *ApJ*, **823**, 70
 Waters, L. B. F. M., Molster, F. J., de Jong, T., et al. 1996, *A&A*, **315**, L361
 Wetzell, S., Pucci, A., & Gail, H.-P. 2012, *J. Chem. Eng. Data*, **57**, 1594
 Woolf, N. J., & Ney, E. P. 1969, *ApJ*, **155**, L181
 Wurm, G., & Blum, J. 1998, *Icar*, **132**, 12
 Yamamoto, T., & Hasegawa, H. 1977, *PTThPh*, **58**, 816
 Zel'dovich, J. B. 1942, *J. Exp. Theor. Phys.*, **12**, 525